
This is an electronic reprint of the original article.
This reprint may differ from the original in pagination and typographic detail.

Girard, J. P.; Lake, R. E.; Liu, W.; Kokkonen, R.; Visakorpi, E.; Govenius, J.; Möttönen, M.
Cryogenic sensor enabling broad-band and traceable power measurements

Published in:
Review of Scientific Instruments

DOI:
[10.1063/5.0143761](https://doi.org/10.1063/5.0143761)

Published: 01/05/2023

Document Version
Publisher's PDF, also known as Version of record

Published under the following license:
CC BY

Please cite the original version:
Girard, J. P., Lake, R. E., Liu, W., Kokkonen, R., Visakorpi, E., Govenius, J., & Möttönen, M. (2023). Cryogenic sensor enabling broad-band and traceable power measurements. *Review of Scientific Instruments*, 94(5), 1-11. Article 054710. <https://doi.org/10.1063/5.0143761>

This material is protected by copyright and other intellectual property rights, and duplication or sale of all or part of any of the repository collections is not permitted, except that material may be duplicated by you for your research use or educational purposes in electronic or print form. You must obtain permission for any other use. Electronic or print copies may not be offered, whether for sale or otherwise to anyone who is not an authorised user.

RESEARCH ARTICLE | MAY 25 2023

Cryogenic sensor enabling broad-band and traceable power measurements

J.-P. Girard ; R. E. Lake  ; W. Liu ; R. Kokkonen ; E. Visakorpi; J. Govenius ; M. Möttönen 



Rev Sci Instrum 94, 054710 (2023)

<https://doi.org/10.1063/5.0143761>



View
Online



Export
Citation

CrossMark

Cryogenic sensor enabling broad-band and traceable power measurements

Cite as: Rev. Sci. Instrum. 94, 054710 (2023); doi: 10.1063/5.0143761

Submitted: 26 January 2023 • Accepted: 1 May 2023 •

Published Online: 25 May 2023



View Online



Export Citation



CrossMark

J.-P. Girard,^{1,2}  R. E. Lake,^{2,a)}  W. Liu,^{1,3}  R. Kokkonen,^{1,3}  E. Visakorpi,¹ J. Govenius,^{1,4} 
and M. Möttönen^{1,4} 

AFFILIATIONS

¹QCD Labs, QTF Centre of Excellence, Department of Applied Physics, Aalto University, P.O. Box 13500, FIN-00076 Aalto, Finland

²Bluefors Oy, Arinatie 10, 00510 Helsinki, Finland

³IQM, Keilaranta 19, FI-02150 Espoo, Finland

⁴VTT Technical Research Centre of Finland Ltd. & QTF Centre of Excellence, P.O. Box 1000, 02044 VTT, Finland

^{a)} Author to whom correspondence should be addressed: russell.lake@bluefors.com

ABSTRACT

Recently, great progress has been made in the field of ultrasensitive microwave detectors, reaching even the threshold for utilization in circuit quantum electrodynamics. However, cryogenic sensors lack the compatibility with broad-band metrologically traceable power absorption measurements at ultralow powers, which restricts their range of applications. Here, we demonstrate such measurements using an ultralow-noise nanobolometer, which we extend by an additional direct-current (dc) heater input. The tracing of the absorbed power relies on comparing the response of the bolometer between radio frequency and dc-heating powers traced to the Josephson voltage and quantum Hall resistance. To illustrate this technique, we demonstrate two different methods of dc-substitution to calibrate the power that is delivered to the base temperature stage of a dilution refrigerator using our *in situ* power sensor. As an example, we demonstrate the ability to accurately measure the attenuation of a coaxial input line between the frequencies of 50 MHz and 7 GHz with an uncertainty down to 0.1 dB at a typical input power of -114 dBm.

© 2023 Author(s). All article content, except where otherwise noted, is licensed under a Creative Commons Attribution (CC BY) license (<http://creativecommons.org/licenses/by/4.0/>). <https://doi.org/10.1063/5.0143761>

I. INTRODUCTION

Historically, the radio frequency (rf) power has been defined by a substitution to electrical direct-current (dc) standards,¹ the Josephson voltage standard, and the quantum Hall resistance standard and, therefore, relies on calorimetric techniques. The International System of Units (SI) was redefined in 2018 through the fundamental physical constants, which has inspired traceable measurements of rf power using radiation pressure² and Rydberg atom sensors.³ According to this redefinition, also the above-mentioned dc substitution provides a traceable path to the SI. It has been a common method for measuring microwave power in room temperature bolometers.^{4,5} Furthermore, the substitution has been utilized to calibrate low-temperature bolometers, for example, for x-ray detection⁶ and astronomical instruments.^{7,8} In astronomy, detectors may be calibrated using atmospheric models and reference black-body calibration sources, such as Mars.⁹ In the optical regime where

single-photon detection is relatively standard due to the high photon energy, the detectors can be calibrated using, for example, heralded photons.¹⁰ Bolometers used in particle detectors are typically calibrated using radioactive sources.^{11–13} However, the traceable calibration technique we use in this manuscript is, in principle, applicable to all of the above cases.

Traceability to the SI at low power, typically below -70 dBm, may be challenging, as it falls below the operating power range of typical commercial power sensors.¹⁴ Nevertheless, emerging technological regimes, such as those based on solid state-qubits, would benefit greatly from accurate measurements of very low microwave power levels in a cryogenic environment. Microwave probe powers for superconducting qubit and spin qubit systems are typically in the range of -120 dBm and -80 dBm, respectively.¹⁵ Very low microwave drive power levels are required in the case of coherent superconducting devices since it is essential to attenuate the thermal noise floor well below the single-photon noise temperature.^{15–18}

Currently, calibration of rf power in the cryostats, widely used in quantum technology with heavily attenuated lines, is inconvenient since the high attenuation calls for characterization of the wiring in different segments,^{19,20} yet the components are physically inaccessible when the cryostat is cold. In addition, if one has only a room temperature power meter, the signal has to be taken back from cryogenic temperatures to the room temperature. Since the lines are typically heavily attenuated, this requires amplification and calibration of the gain of the amplification chain, which adds uncertainties and noise to the measurement. For example, for this reason, we recently introduced a method of calibrating the gain of cryogenic amplification chains,²¹ but yet a cryogenic power sensor seems more appealing for measuring rf power at low temperatures.

Devices used in circuit quantum electrodynamics^{22,23} (cQED) call for accurate characterization of the ambient radiation and their microwave properties at ultralow power levels. Experiments in cQED are based on superconducting circuits that use nonlinear elements, i.e., qubits, which operate mainly between 100 MHz and 20 GHz^{24–27} and at a low signal level to prevent unwanted artifacts, such as alternating-current (ac) Stark shifts.^{28,29} In this context, there is a strong incentive to develop efficient and practical detectors operating in the microwave range. Although some detectors for itinerant microwave photons recently managed to reach single-photon sensitivity with efficiencies up to 96%,^{30–33} they rely on discrete qubit transitions or on cavity-confined photons to facilitate detection.^{34,35} This limits signal amplitude calibration to a rather narrow relative bandwidth³⁶ with the possibility of extending it to 1 GHz by observing a high-level ac Stark shift in a multilevel quantum system with a large frequency detuning,^{37,38} but this extension comes at the cost of reduced energy sensitivity. Another method³⁹ enables absolute calibration of power over a gigahertz-wide frequency range by measuring the spectra of scattered radiation from a two-level system in a transmission line. In addition, *in situ* characterization of qubit control lines in the megahertz regime has been implemented⁴⁰ using a transmon qubit coupled to a readout resonator. Analyzing the power dependence of the magnitude of the reflection coefficient at resonance of a tunable transmon-type superconducting circuit has also recently been employed as a radiation field thermometer.⁴¹ Overall, it is especially challenging to characterize ultralow microwave power at unknown frequencies and levels.

Despite the great progress that has been accelerated by the race for a useful quantum computer, experiments in cQED usually lack tools to achieve reliable traceable power absorption measurements over a broad relative frequency band and over a range from fractions of photons to several photons in the frequency band of the signal. This tool gap hinders the accuracy and speed of key characterization measurements and, hence, introduces limitations for the operation characteristics of quantum-technological and other cryogenic devices. Consequently, there is an urgent need for new tools to fill the gap in implementing the standard for ultralow rf power. In this work, we introduce a traceable power absorption measurement based on dc substitution to enable high-precision measurements and, furthermore, provide a simple way to calibrate microwave power in a cryogenic environment. For this purpose, we deem bolometers to be a promising candidate because of their naturally broadband low-temperature input, low operation power, small size, and simplicity. They can even achieve remarkable sensitivity, since recent studies suggest that ultralow-noise bolometers

based on the Josephson effect may enable calorimetric measurement of itinerant microwave photons in the framework of cQED.^{42,43}

II. DETECTION SCHEME

The application of bolometers in the gigahertz regime^{44,45} has required the development of nanoscale thermal absorber elements with reduced heat capacity achieved through optimization of both device geometry and materials.⁴⁶ Therefore, methods of electronic thermometry in mesoscopic devices are directly relevant for the thermal detection mechanisms.⁴⁷ In particular, rf reflectometry of a circuit with a temperature-dependent impedance offers fast readout with low-back-action from the rf probe.⁴⁸

This article further describes a thermal detection approach that uses superconductor–normal-metal–superconductor (SNS) junctions as the temperature-dependent impedance.^{42,49–51} As the temperature of the normal-metal region of an SNS element increases, its Josephson inductance increases, which is observed experimentally as the lowering of the resonance frequency of a tank inductance-capacitance (LC) resonator. In the device, electrical properties of the SNS junction are governed by the length and diffusion constant of the normal-metal weak link itself rather than the superconducting leads.^{52–54} The minigap in the density of quasiparticle states is strongly temperature-dependent even for temperature excursions of a few millikelvin.⁵⁵ At frequencies corresponding to energies below the minigap, a low-power microwave signal can be used to probe the superconducting critical current in the SNS junctions. This quantity depends on the electron temperature.

For the SNS junctions in our bolometers, we estimate that the characteristic energy scale of the proximity effect, i.e., the Thouless energy, is $E_T = \hbar D l^{-2} = h \times 13.5$ GHz, where the diffusion constant is $D \approx 35.8$ cm² s⁻¹, the length of the normal-metal junction region is $l \approx 200$ nm, and \hbar is the reduced Planck constant ($h/2\pi$). At low temperatures, the corresponding predicted minigap is $E_g \approx 3.1 \times E_T$, which imposes an upper bound on design of the useable probe bandwidth.⁵⁶ In the implementation below, the probe frequency is designed to be near 500 MHz to avoid dissipation from the bolometer readout that may occur from driving at frequencies higher than the frequency corresponding to the minigap.⁵³

Other schemes have utilized measurements of the temperature-dependent switching current of a Josephson junction to probe local heating of an SNS junction.^{43,50} The method we describe in this article stems from an identical physical phenomenon even though we use an rf probe, i.e., the decrease in the critical current I_C is equivalent to an increase in the Josephson inductance⁵⁷ L_J , ideally as $I_C = (\Phi_0/2\pi)/L_J$, where Φ_0 is the magnetic-flux quantum. In addition, the real part of the junction admittance increases when temperature is increased, but this effect is comparatively weak when the probe frequency and bath temperature remain below the minigap energy.^{49,53,58} The devices are probed with an rf signal that pushes current through the junction at a level below its critical current, and hence, the junction never switches to the normal-state during the measurement.

Figure 1 shows our implementation of a bolometer for accurate traceable microwave power detection in the cryogenic environment. Additional details on sample fabrication are reported in Appendix A. The device has three distinct key components: (i) a thermal absorber, (ii) a readout circuit, and (iii) a dc heater, each of which we describe

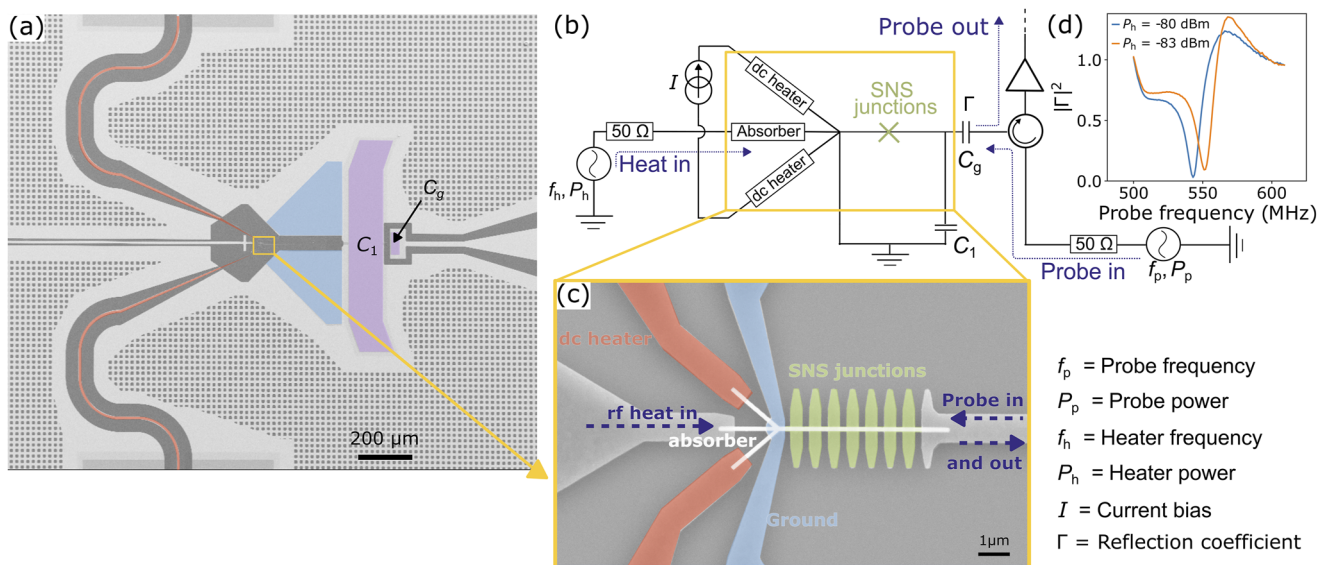


FIG. 1. Description of the bolometer sample. (a) False-color optical image of the bolometer with a dc heater. The traceable electrical current is applied to the heater through a dc-heater line (red), and the sample is grounded through aluminum leads (blue). (b) Circuit diagram of the measurement setup indicating the shunt capacitor C_1 and gate capacitor C_g also shown in (a) in purple. (c) False-color scanning-electron-microscope image of the detector. The long junctions operating as resistive power absorbers are 1- μm long, and the short junctions operating as the thermometer are 300-nm long. The superconductor–normal-metal–superconductor (SNS) junctions operating as the thermometer are formed by a AuPd nanowire (white) galvanically connected to superconducting Al islands and leads. The absorber is either heated by the microwave heater signal or by the dc heater. (d) Fraction of the probe power reflected at the gate capacitor as a function of probe frequency for heater powers of -80 dBm (blue) and -83 dBm (orange) at the absorber. An increase in the heater power induces a redshift of the resonance frequency.

below. The central element of the bolometer is a continuous normal-metal–gold–palladium ($\text{Au}_x\text{Pd}_{1-x}$) nanowire that is shown in detail in Fig. 1(c). The nanowire is contacted by superconducting Al electrodes at various locations. The chemical composition of the normal-metal nanowire is reported in Appendix B. The micrograph of Fig. 1(c) is color-coded to indicate the leads of the dc heater (red), the ground electrode (blue) to separate electrically the absorber from the readout, and the aluminum islands (green) to induce proximity superconductivity in the readout section. Both leads of the dc heater in Fig. 1(c) fan out to a pair of on-chip bond pads that enable a four-wire resistance measurement of the dc heater and accurate detection of the current bias through the circuit (see Appendix A).

In Fig. 1(c), the thermal absorber is comprised of the left section of nanowire that is longer than the coherence length of the superconducting aluminum thin film.⁵⁹ In fact, the absorber is designed to be a matched resistor that can terminate a microwave transmission line with a characteristic impedance of $Z_0 = 50 \Omega$ to absorb rf power. In the measurements that are described below, the microwave heater signal is provided by a room temperature signal generator and is delivered through 50Ω coaxial transmission lines with thermalized filters and attenuators to the 10 mK base temperature stage of the cryostat. Once the signal reaches the sample, it is absorbed by the nanowire, increasing its temperature.

In contrast to the absorber, the readout circuit of the bolometer [Figs. 1(a)–1(c)] is made up of a series of eight shorter SNS junctions that assume reactive electrical behavior due to the presence of a minigap and finite Josephson inductance within each weak link. In practice, the Josephson junction symbol denoted as “X” in Fig. 1(b)

is realized physically as the series of eight SNS junctions shown in Fig. 1(c). In order to achieve readout with rf reflectometry, the series of eight SNS junctions is placed in parallel with an on-chip capacitance C_1 to ground to realize an LC readout circuit resonating at $f_r \sim 500$ MHz. We probe the readout circuit using a low-power microwave probe so that the SNS junctions are well approximated as a linear inductor.⁴⁹ Since heating increases the inductance of the SNS junctions, the resonance frequency shifts down with increasing heating power, as shown in Fig. 1(d). Importantly, the thermal absorber and the readout circuit are electrically decoupled from one another by the central electrode that shunts the center of the nanowire to ground, i.e., the probe tone does not dissipate at the absorber and dc heater. However, since both the probe and absorber sections are formed by a common nanowire, these sections are thermally connected and defined by a single temperature on the relevant timescales, but we note that temperature equilibration throughout the nanowire is not necessary when operating the dc substitution method described below. The correct operation requires only an identical response at the thermometer from the two different heating types. Based on an experimental study of metallic wires with similar dimensions and at similar temperatures,⁶⁰ we expect the quasiparticles to quickly relax and reach thermal quasi-equilibrium at least within a nanosecond timescale. Additional discussion on the thermal conductance of the detector is reported in Appendix C.

The calibration of the rf power absorbed at the device is described in detail in Secs. IV and V. In a nutshell, we first apply a dc-heater current inducing heating on the order of a few femtowatts and observe the corresponding change in the reflection spectrum of

the probe signal. Next, we sweep the rf heater power (and frequency) and record the response of the probe reflection. With these data, we can carry out a dc substitution method to calibrate the rf power delivered to the absorber by minimizing the residuals between the acquired probe reflection spectrum under dc and rf heating. Importantly, we can establish a path to metrological traceability for the rf heating power even at extremely low levels because we can utilize the pre-calibration of the room temperature voltage source and of the resistors used to generate the dc-heater current.

To measure microwave power at room temperature, a typical experiment using a low-temperature detector requires an accurate calibration of the attenuation of the rf line, through which the heater signal is applied. Figure 2 shows a detailed diagram of our experimental setup. Multiple attenuators, amplifiers, filters, and directional couplers are placed between the sample and the instruments to enhance the signal-to-noise ratio. This setup enables us to accurately

measure the power that is transmitted at frequency f_h from room temperature through the cabling and into the broadband cryogenic power sensor at the base temperature of the dilution refrigerator.

On the right in Fig. 2, we show the electronics and wiring for probing the resonant readout circuit of the bolometer. The probe signal is input through an attenuated coaxial line and filters and sent through the coupled port the directional coupler installed at the base temperature stage. The probe signal impinges on the readout circuit and is reflected back through the main line of the directional coupler, where it is amplified by a cryogenic high-electron-mobility amplifier installed on the 4 K stage. The recorded signal represents the transmission spectrum (S_{21}) through the rightmost pair of lines in Fig. 2, but the key feature in the data is the dip that arises from the reflection from the readout circuit. Therefore, in the discussion below, we refer to the readout signal as a reflection spectrum. We set the readout power low enough so that the readout resonance is

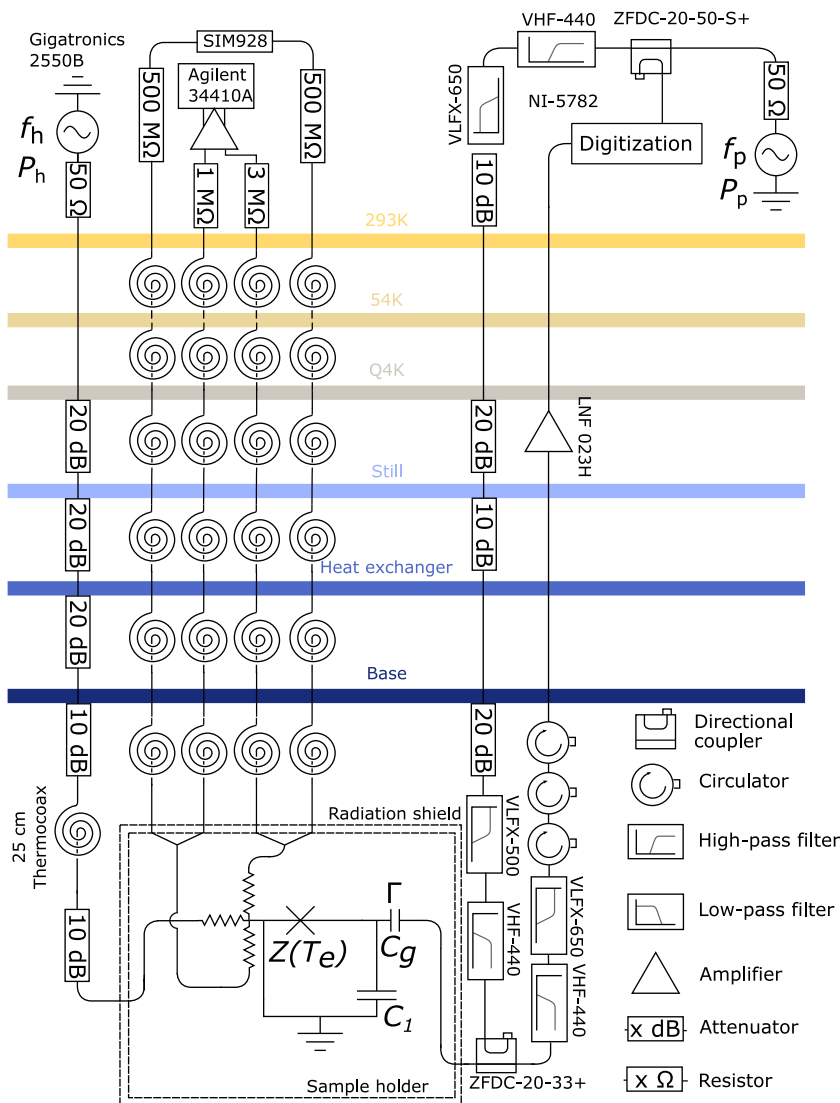


FIG. 2. Main experimental setup for a traceable power absorption measurement with a bolometer equipped with a dc heater. The sample is placed inside a radiation shield to mitigate external noise. Thermalization of the lines going down to the base temperature of the cryostat is ensured by the presence of additional cable length (spiral shape) between each temperature stage.

Downloaded from http://pubs.aip.org/aip/rsi/article-pdf/doi/10.1063/5.0143761/17815661/054710_1_5.0143761.pdf

in the linear response regime, i.e., the readout resonance frequency is invariant to small changes in the probe power. When considering the attenuation and coupling scheme of Fig. 2, the power delivered to the probe circuit is approximately -90 dBm (1 pW) at the frequency of 550 MHz in these measurements. Probe power remains constant during a calibration and measurement routine.

The specifications provided for the commercial devices in Fig. 2 give a rough estimate of the line attenuation, but a more careful investigation is needed since many of the components are specified to work at or near room temperature. Attenuations can be measured with a vector network analyzer (VNA), but this can be difficult with heavily attenuated rf lines. Furthermore, VNA measurement necessarily includes attenuation, or gain, of the return path. This can be circumvented to some extent by measuring the gain of the return path with the so-called Y-factor technique.

The presence of a dc heater at the bolometer enables us to bypass these limitations by carrying out detection *in situ* at the base temperature stage of the dilution refrigerator. Instead of a full setup calibration, we only need to determine the response of the bolometer as a function of the dc heater power. Note that this method can be applied without changing the base temperature of the cryostat. Therefore, our results reveal the amount of microwave power absorbed very close to the quantum device.

The 1σ uncertainty estimates of the different instrument calibrations and of the derived quantities are given in Table I. We

TABLE I. Uncertainty estimates (1σ) of the different instrument calibrations.

Instrument or derived quantity	Linear uncertainty (%)	Logarithmic uncertainty (dB)
SIM 928	0.016	0.0007
Voltmeter	0.003	0.0001
Amplifier gain @ 60 dB	0.4	0.02
1-G Ω reference resistor	0.04	0.0017
1-G Ω resistor	0.06	0.0026
Gigatronics 2550B @ 100 MHz	9.6	0.42
dc heater power	1.1	0.05

assume uncertainties to be independent, and hence, we added them in squares for derived quantities. Furthermore, we transformed between the linear (U_{lin}) and logarithmic (U_{log}) uncertainties using the equation $U_{\text{log}} = 10 \log_{10}(e) \times U_{\text{lin}}$ dB, where e is Euler's number.

III. MEASUREMENT

We examine the performance of the bolometer in terms of its noise equivalent power (NEP), which is a typical figure-of-merit for bolometers and is defined as the noise in the bolometer readout signal in the units of the bolometer input power. Example measurement data from the NEP extraction process are shown in Fig. 3. Specifically, to determine the NEP, we follow the procedure described in our previous work⁶¹ by first measuring the voltage noise spectrum of the output signal [Fig. 3(a)] and then dividing it by the quasistatic responsivity of the detector [Fig. 3(b)]. We further take into account the frequency dependence of the responsivity by dividing the quasistatic responsivity by a factor $\sqrt{1 + (2\pi f_n \tau)^2}$, where τ is the measured time constant of the detector and f_n is the noise frequency. The time constant is obtained by an exponential fit to the excursion of the probe signal upon the delivery of microwave heater power to the “heat in” port of the device, as shown in Fig. 3(b). This procedure yields the noise of the bolometer output in units of the input power, which we take as the definition of NEP. The experimental data shown in Fig. 3(c) indicate that the lowest measured NEP is roughly $2 \text{ aW}/\sqrt{\text{Hz}}$, together with a $20 \mu\text{s}$ thermal time constant. For power sensing, the thermal time constant suggests a maximum repetition rate of the order of ten kHz. To measure, for example, an incoming power of 10 fW at a relative uncertainty of 1%, one needs an integration time of 0.2 ms according to the measured NEP, which is not limited by the thermal time constant. The measured NEP is roughly two orders of magnitude greater than that previously reported⁶¹ on similar sample without a dc heater. This difference can be explained by the roughly three times larger volume of the metal in the dc bolometer and, perhaps more importantly, by the presence of two dc lines, inducing an additional low-frequency noise channel for the sample. For example, the triboelectric and piezoelectric effects can introduce noise even in unbiased wires, and if the

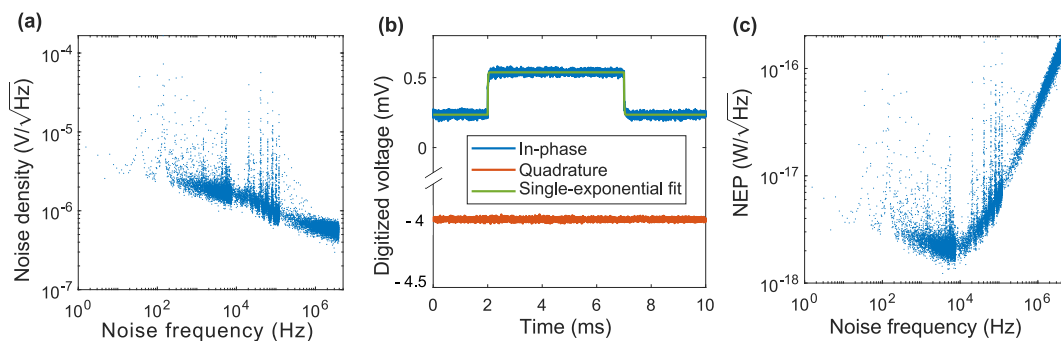


FIG. 3. (a) Spectral density of voltage noise measured for the bolometer probe signal. (b) Time trace of the in-phase (blue) and quadrature (red) voltage of the measured probe signal for the heater power turned on at the time $t = 2$ ms and turned off at $t = 7$ ms. The green line denotes a single-exponential fit of the in-phase part. (c) Noise equivalent power (NEP) of the bolometer as a function of noise frequency.

wires are voltage biased, the change in their capacitance owing to vibrations promotes current noise.

Using method I or II described below, one needs to carry out several measurements of the reflection coefficient to measure the attenuation of the cabling. In our current experiment, we sweep the rf heater power and compare it to a single dc heater power. Alternatively, to determine the power of an unknown signal, one can use calibration data for the reflection coefficient at different dc heater powers. Note that if one has obtained beforehand such calibration data, then the total measurement time is limited to the acquisition of a single trace of the transmission coefficient.

IV. RESULTS: METHOD I

In the following, we present in detail our calibration method. First, we measure over a range of probe frequencies f_p the transmission coefficient S_{21} of the probe signal, from the source to the digitization stage shown in Fig. 2, with finite dc heating such that the resonance shifts by ~ 1 MHz with respect to the zero-bias case. Next, we repeat the measurement at zero dc-heater power but at a considerable output power of the rf heater signal generator and calculate the sum of the squared differences between the rf-heating trace $S_{21}^{rf}(f_p)$ and the dc-heating $S_{21}^{dc}(f_p)$, i.e., we define the residual as

$$R_0 = \sum_{f_p} \left(\left\{ \text{Re}[S_{21}^{dc}(f_p)] - \text{Re}[S_{21}^{rf}(f_p)] \right\}^2 + \left\{ \text{Im}[S_{21}^{dc}(f_p)] - \text{Im}[S_{21}^{rf}(f_p)] \right\}^2 \right). \quad (1)$$

A small residual indicates nearly equal absorbed power induced by the rf and dc heating sources.

In Fig. 4(a), we show the residual as a function of the applied rf power to the heater line. We find the rf power corresponding to the dc-heater power by fitting a third-order polynomial to the data near the minimum. Our fitting routines are available online.⁶¹ Near the minimum, where the spectra from dc and rf heating approach equivalence, Eq. (1) behaves as a parabola. A weak asymmetry emerges when rf and dc powers deviate, motivating the use of the third-order fit function to accurately determine the location of the minimum. We repeat such measurements six times to estimate the statistical uncertainty of the measurement.

The heater line is comprised of commercial silver-plated cupronickel coaxial cables, cryogenic microwave attenuators, and a 25-cm Thermocoax cable with a 0.5-mm-diameter inner conductor.⁶² As expected, we observe in Fig. 4(b) a strong frequency dependence in the attenuation of the heater line dominated by the Thermocoax cable. However, at low frequencies where the coaxial conductor losses are small, we find that the attenuation approaches the cumulative nominal value of the added attenuation present in the setup (80 dB). For increasing frequency in Fig. 4(b), losses further increase and exceed 120 dB at 7 GHz. The demonstrated ability to resolve frequency-dependent microwave loss that exceeds 75 dB from room temperature to cryogenic conditions highlights a major advantage of our methodology with respect to the current state of the art. For example, without a cryogenic power sensor, a measurement needs to be carried out by connecting a pair of nominally identical heater lines at the base temperature stage with a loop-back connection, measuring the round-trip transmission with a network

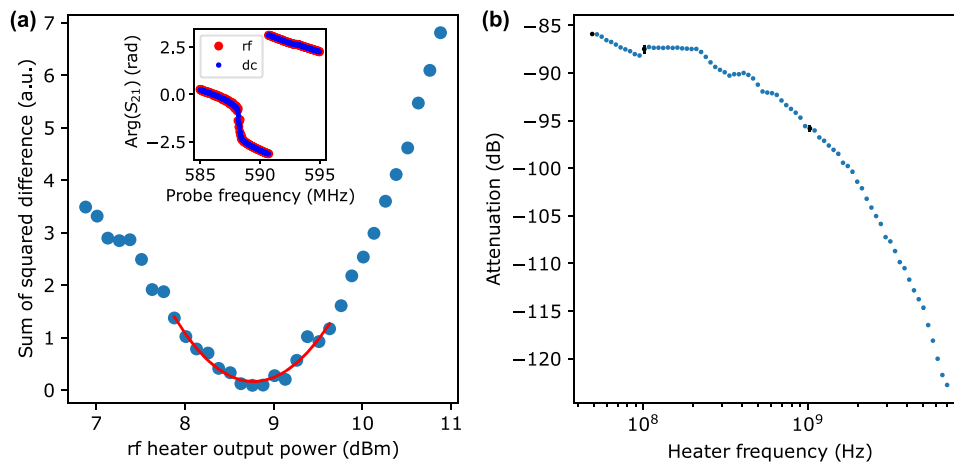


FIG. 4. Comparison of probe response curves used to deduce the equivalence between dc and absorbed rf heating powers. (a) Example of the sum of squared differences of the complex-valued probe S-parameter coefficient S_{21} as a function of the applied rf heater power generated by a signal generator at a 7-GHz frequency for an applied dc heater power of -114.03 dBm. The minimum of the fitted third-order polynomial function is achieved at 8.77 dBm. The attenuation at 7 GHz is -122.80 dB, of which 0.55 dB arises from the imperfect matching of the rf absorber impedance to the $50\text{-}\Omega$ transmission line. Inset: phase of S_{21} as a function of probe frequency for dc and rf heating and 8.75 dBm of applied rf heating. (b) Attenuation of the rf-heater line as a function of the heater signal frequency. The strong frequency dependence is due to a Thermocoax cable used in the setup. The black markers indicate discrete frequencies where output power of the microwave source was calibrated using a commercial power meter. The uncertainty of the attenuation at the black markers is provided in Table II. The data corresponding to the blue markers lack the calibration of the source and, hence, has a greatly elevated uncertainty.

analyzer and subsequently dividing the transmission magnitude by two in order to infer the average insertion loss per line. However, a commercial network analyzer has a dynamic range of ~ 154 dB for frequencies of 3.5–10 GHz (cf. Table XI in Ref. 63). Consequently, if a pair of heater lines from the present work were looped together from the base temperature stage, the round trip attenuation would not be resolvable under these typical measurement conditions with standard room temperature electronics.

The 1σ confidence interval of the type A uncertainty of the measured attenuation is below 0.1 dB for ~ 10 min of measurement time. Figure 4(b) indicates the discrete frequencies (50, 100 MHz, and 1 GHz) where the output power of the Gigatronics room temperature microwave generator was calibrated using a commercial room-temperature microwave power meter (see Appendix D and Table II). Below, we estimate the uncertainty of the measured attenuation at these frequencies. Outside these frequencies, we do not give a precise estimation of the uncertainty, which is likely of the order of a few decibels.

In addition to the noise in the measurement, we have systematic error arising from the calibration of our instruments. The current bias is provided by a Stanford Research Systems SIM 928 voltage source with nominal 0.5-G Ω resistors in both dc lines. The total measured resistance is $0.9955 \text{ G}\Omega \pm 0.6 \text{ M}\Omega$. The SIM voltage source has an uncertainty of 160 ppm. The dc lines and the on-chip dc heater resistors have resistances well below 1 k Ω . The effect of the resistors on the bias current can be neglected without loss of accuracy.

We measured the resistance of the dc-heater resistors in a four-probe configuration using an Agilent digital multimeter model 34410A as a voltmeter. The voltage was amplified with a Femtoamp DLPVA-100 voltage amplifier, and the nominal 60-dB gain was measured to be 60.02 ± 0.0013 dB. The resistance of the heater R_{heater} determined from the slope of the measured current–voltage curve yields $(48.8 \pm 0.5)\Omega$. The dc power reaching the bolometer has an uncertainty of ~ 0.05 dB, which is limited by noise and the uncertainty of the dc-heater resistance.

TABLE II. Uncertainty estimates (1σ) for the bolometer readout, the power output of the microwave signal generator (Gigatronics 2550B), and the resulting measured attenuation for the black points in Fig. 4(b).

	Heater frequency		
	50 MHz	100 MHz	1 GHz
Statistical uncertainty			
Linear (%)	1.2	1.9	0.6
Logarithmic (dB)	0.05	0.08	0.03
Gigatronics 2550B uncertainty			
Linear (%)	1.6	9.6	8.4
Logarithmic (dB)	0.07	0.42	0.36
Attenuation uncertainty			
Linear (%)	2.29	9.88	8.31
Logarithmic (dB)	0.1	0.43	0.36

Consequently, we observe that at 100 MHz, the uncertainty of the measured attenuation in Fig. 4(b) is clearly dominated by that of the room temperature microwave source, 0.33 dB. At 50 MHz and 1 GHz, the uncertainty of the attenuation is greatly improved owing to only 0.01-dB contribution from the microwave source, and hence, it is dominated by the 0.1 dB statistical uncertainty of the measurement.

We observe several unexpected features in Fig. 4(b), such as plateaus, with kinks and a sharp drop of the attenuation just before 100 MHz. We attribute these to the room temperature microwave source, which is not accurately calibrated at these frequencies. The drop in the attenuation is likely reminiscent of a drop of roughly 2 dB in the output power of the microwave source in the vicinity of 100 MHz. In the future, the accuracy of the attenuation measurement in the whole frequency range can be conveniently improved by a fully calibrated microwave source. However, we note that the source uncertainty only affects the attenuation measurement, not the measurement of the absorbed rf power at cryogenic temperatures. Further calibration details are provided in Appendix D.

Finally, we correct systematically all data points in Fig. 4(b) to account for the power reflected (and not absorbed) due to the impedance mismatch between the heater line and the absorber. The incomplete absorption of the incident heater power artificially increases the measured attenuation of a line. We extract the resistivity of the normal-metal wire (Appendix A, Fig. 6), deduce the resistance of the absorber, and calculate the incident power that is reflected. For this sample, the absorber resistance is determined to be $R = 24.4 \Omega$, which corresponds to a reflection of 0.54 dB of power from the 50- Ω heater line. The attenuation results of Fig. 4(b) have been corrected by adding the reflected power (0.54 dB) to the raw data. Future studies should address precision measurements of microwave scattering parameters over broader frequency ranges, especially in the ultra-low power regimes, to further improve determination of detector coupling efficiency.^{20,64} Note that it is also possible to measure the impedance mismatch by a microwave reflection measurement at the heater input. Furthermore, it is straightforward to achieve absorber resistance consistently in the range of 40–50 Ω .

V. RESULTS: METHOD II

Alternatively, we can calibrate the rf heater power by measuring the resonance frequency at multiple dc-heater currents and output powers of the rf-heater signal generator, as shown in Fig. 5. Finding the offset between the dc and rf heater powers that minimizes the difference between the resonance frequencies measured with the two heating methods yields the attenuation of the heater line. A similar method can be applied to quantities other than the resonance frequency. For example, we can measure the transmission coefficient at a given frequency as a function of dc and rf heater powers. In this case, the attenuation of the rf line is the offset power that minimizes the difference between the two transmission coefficients. However, we deem method II to be less robust since it does not utilize the full information on the resonance. Nevertheless, such a method could be greatly faster than the one we use above and remains an appealing line of future research. The primary measurement results of

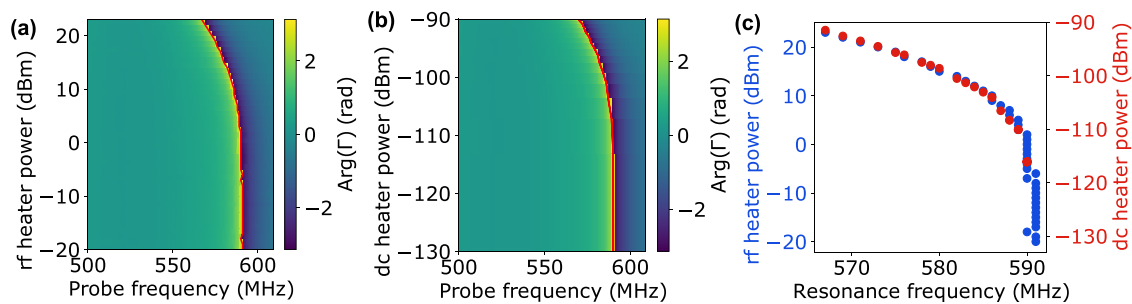


FIG. 5. Deduction of the attenuation of the heater line with method II. Phase of the reflection coefficient Γ as a function of the probe frequency and the (a) rf and (b) dc-heater power. The resonance frequency is depicted by the red line. (c) Comparison of the resonance frequencies obtained by the dc and rf heating at $f_h = 5$ GHz. In this example, the best match between the two curves is obtained when considering -114.3 dB attenuation along the rf-heater line.

Fig. 4(b) and Tables I and II are only from the method I reported in Sec. IV.

VI. DYNAMIC RANGE

From Fig. 5(c), we can also obtain an indication of the dynamic range of our power sensing technique using method II, which exceeds 20 dB for the configuration given by the wiring of Fig. 2. The dynamic range is limited from above by the maximum output power of the room temperature Gigatronix source owing to the high total line attenuation. Otherwise, the trend of decreasing resonance frequency of the readout with increasing heating power could be extended further by increasing the microwave power delivered to the bolometer. Therefore, Fig. 5(c) highlights a potential advantage of thermal detection with respect to qubit-based photon detection schemes discussed in Sec. I, i.e., this type of bolometer can resolve power levels spanning those corresponding to a few microwave photons on average (attowatts),^{42,65} to higher input powers, up to several picowatts as demonstrated in the present article.

VII. CONCLUSIONS

In summary, we developed a sensitive bolometer device for traceable microwave power absorption measurements relying on dc substitution. The device operates at low temperatures, exhibits a broad input bandwidth, and is suitable for characterization of devices operating in the framework of cQED. As an illustration of the utility of the introduced microwave sensor, we demonstrated the calibration of a heavily attenuated rf line, including several microwave components at low temperatures. We achieved this by comparing the response of the bolometer to a heater signal applied through the rf line and to heating applied through a dc line. From this comparison, we accurately determined the frequency-dependent attenuation of the rf line with an uncertainty of 0.1 dB for an absorbed power of -114 dBm. We note that this method potentially leads to a substantial time reduction in setup characterization compared with the so-called Y-factor method that requires one to change the temperature of a resistor and consequently to wait for potentially slow saturation of the thermal relaxation. This work aims to facilitate the implementation of bolometers in experiments on cryogenic electronics as traceable power sensors and to

enable highly accurate power measurements. From the noise performance of the device, we observed that the sample would benefit from improved shielding from dc-line noise, and in future experiments, we plan to use such a bolometer for microwave signal calibration in qubit experiments, both for investigations of readout with thermal detectors⁶⁶ and pre-qualification of qubit wiring schemes through accurate measurements of line attenuation and noise power that reaches the sample space.¹⁷

ACKNOWLEDGMENTS

We acknowledge the provision of facilities and technical support by Aalto University at OtaNano–Micronova Nanofabrication Center and LTL infrastructure, which is part of the European Microkelvin Platform (EMP, Grant No. 824109 EU Horizon 2020). We have received funding from the European Research Council under Consolidator Grant No. 681311 (QUESS) and under Advanced Grant Nos. 670743 (QuDeT) and 101053801 (ConceptQ), the European Commission through H2020 program projects QMiCS (Grant Agreement No. 820505, Quantum Flagship), the Quantum Flagship funding by the European Commission through Project No. 101113946 (OpenSuperQPlus100), the Academy of Finland through its Centers of Excellence Program (project Nos. 312300, 312059, and 312295) and grants (Nos. 336810, 314447, 314448, 314449, 305237, 316551, 308161, 335460, and 314302), the Finnish Cultural Foundation, the Vilho, Yrjö, and Kalle Väisälä Foundation of the Finnish Academy of Science and Letters, the Jane and Aatos Erkko Foundation, and the Technology Industries of Finland Centennial Foundation.

AUTHOR DECLARATIONS

Conflict of Interest

M.M. declares that he is a Co-Founder and Chief Scientist of the Quantum-Computer company IQM. R.E.L., R.K., and M.M. declare that they are inventors in a related family of patents titled *Cryogenic microwave analyzer* (patent application number FI20176051A and herein) owned by IQM Finland Oy. The other authors have no conflicts to disclose.

Author Contributions

J.-P. Girard: Investigation (equal); Methodology (equal); Validation (equal); Writing – original draft (equal). **R. E. Lake:** Conceptualization (equal); Methodology (equal); Writing – review & editing (equal). **W. Liu:** Investigation (equal). **R. Kokkonen:** Data curation (equal); Investigation (equal). **E. Visakorpi:** Methodology (equal). **J. Govenius:** Conceptualization (equal); Methodology (equal). **M. Möttönen:** Conceptualization (equal); Funding acquisition (lead); Supervision (lead); Writing – review & editing (equal).

DATA AVAILABILITY

The data and analysis scripts are openly available on Zenodo at <https://zenodo.org/record/7804794>.

APPENDIX A: SAMPLE DETAILS

1. Fabrication

We begin with a high-resistivity ($\rho > 10 \text{ k}\Omega \text{ cm}$) four-inch silicon wafer (100) covered by a 300-nm thermal oxide SiO_x and sputter on it 200 nm of pure Nb. We define the waveguide in a Karl Suss MA-6 mask aligner using AZ5214E photoresist in positive mode with hard contact. After development, the sample is etched with the Plasmalab 80Plus Oxford Instruments reactive ion etching (RIE) system. The plasma works with a gas flow of SF_6/O_2 at 40/20 SCCM with a rf-field power of 100 W. After etching, the resist residuals are cleaned in an ultrasonic machine with acetone and IPA and dried with a nitrogen gun. Next, a thin film dielectric layer Al_2O_3 (45 nm) is grown by atomic-layer deposition (ALD) in a Beneq TFS-500 system. The dc-heater dielectric layer is protected using AZ5214E resist, and the rest of the ALD oxide is wet-etched with an ammonium fluoride–hydrofluoric acid mixture. Then, the four-inch wafer is cleaved into a $2 \times 2 \text{ cm}^2$ chip by Disco DADdy. Subsequently, the nanowire is patterned by EPBG5000pES electron beam lithography (EBL) with a bilayer of MMA/PMMA resist on a single chip. The 30-nm-thick AuPd layer is deposited in an e-beam evaporator at a rate of 0.5 \AA/s . After liftoff in acetone overnight, the superconducting leads galvanically connected to the nanowire are patterned by EBL and deposited with 100 nm Al at a rate of 5 \AA/s . Finally, each pixel ($5 \times 5 \text{ nm}^2$) is cleaved by a laser micromachining system and packaged with Al bonding wires.

2. Nanowire resistance

Figure 6 shows the result of a four-wire sensing measurement for the series resistance of the two dc-heater resistors at 10 mK with a two-second integration time and five averages. A constant voltage offset arising from the room-temperature voltage amplifier ($968 \mu\text{V}$) has been subtracted from all data points. As expected, the dc heater behaves as an Ohmic resistor with a linear relationship between the applied current and measured voltage drop. From a linear fit to the data, we obtain a resistance of 48.8Ω .

In addition to the determination of the heater resistance, the data in Fig. 6 combined with the analysis of the feature sizes in the micrograph of Fig. 1(c) enable the extraction of resistiv-

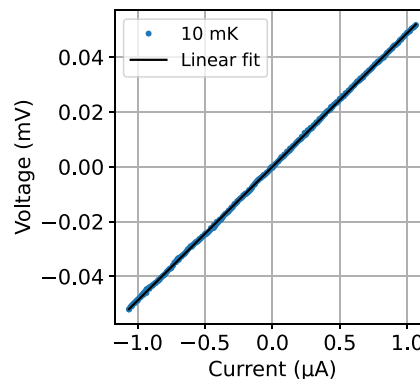


FIG. 6. Voltage drop across the dc heater consisting of two AuPd resistors as a function of the applied current at 10 mK. The voltage amplifier has a fixed offset value of $968 \mu\text{V}$, which has been subtracted from all of the shown data points.

ity, diffusion constant, and Thouless energy. We determine the AuPd wire resistivity to be $\rho = 1.10 \times 10^{-7} \Omega\text{m}$, corresponding to an elastic mean-free path of $l_e = 7.7 \text{ nm}$ and a diffusion constant of $D = v_F l_e / 3 = 3.58 \times 10^{-3} \text{ m}^2 \text{ s}^{-1}$, taking the Fermi velocity to be $v_F = 1.4 \times 10^6 \text{ m/s}$. For the junctions in the readout circuit, this results in the Thouless energy $E_T / \hbar = 13.5 \text{ GHz}$.

APPENDIX B: NANOWIRE CHEMICAL COMPOSITION

We evaluate the chemical composition of the AuPd nanowire by energy dispersive x-ray (EDX) analysis. We find the nanowire composition to be $\text{Au}_x\text{Pd}_{1-x}$ with $x \approx 0.58$. To prevent damaging the measured sample, this study is carried out on different but nominally identical samples fabricated in a different batch. Figure 7 shows the x-ray spectrum. The peaks at 2.121 and 2.838 keV correspond to Au and Pd, respectively. The electron beam energy is set to 5 keV during analysis.

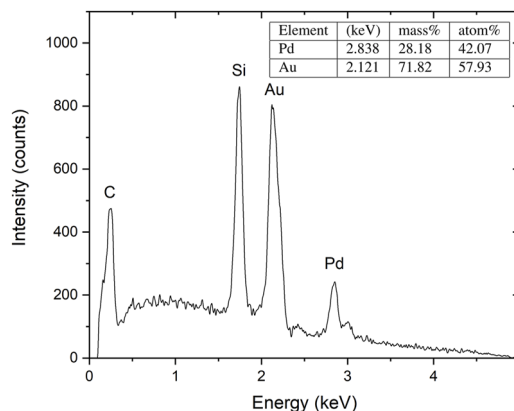


FIG. 7. Energy-dispersive x-ray spectroscopy of the AuPd nanowire of a nominally identical sample to that cryogenically measured in this work.

APPENDIX C: HEAT LOSSES AND THERMAL CONDUCTANCE

Similar to Ref. 67, one can estimate the thermal conductance in the SNS junctions⁶⁸ G_{SNS} and compare it to the thermal conductance to the cryostat phonon bath G_b . To quantify this heat transfer, we consider the ratio $l_s = L_s/\xi_0$, where L_s is the length of the superconducting aluminum between the absorber resistor and the thermometer part of the bolometer and ξ_0 is the superconductor coherence length. We obtain a ratio of $l_s \approx 1$ by considering $\xi_0 = \sqrt{\hbar D_s/\Delta_0}$, where the Al bulk energy gap at zero temperature is $\Delta_0 = 200 \mu\text{eV}$, the diffusion constant of the superconductor is $D_s = 50 \text{ cm}^2/\text{s}$, $L_s = 300 \text{ nm}$, and \hbar is the reduced Planck constant. According to Ref. 67, under these conditions, G_{SNS} can be approximated by the Wiedemann–Franz value $\mathcal{L}_0 G_N T$, with \mathcal{L}_0 being the Lorentz number and G_N being the normal state electrical conductance. This yields a thermal conductance of $G_{\text{SNS}} = 0.4 \text{ nW/K}$, which is more than five orders of magnitude larger than the thermal conductance from the nanowire to the cryostat phonon bath that we previously reported on an otherwise similar device but without the dc heater.⁴⁹ Therefore, we expect the chain of SNS junctions to be strongly thermally coupled to the rf absorber and dc heater.

APPENDIX D: CALIBRATION OF INSTRUMENTS

The voltmeter and the amplifier were calibrated against a Fluke 5440B voltage calibrator, which, in turn, was shortly before the experiments calibrated by VTT MIKES in a way traceable to the Josephson voltage standard. Next, a calibrated voltmeter was used to verify the output voltage of the SIM 928 voltage source. The resistances of the bias resistors were measured with an Agilent 34410A multimeter using a four-probe configuration. The multimeter resistance reading was calibrated against the Measurements International model 4310H resistance standard. An Agilent N1913A power meter was used to verify the output power of the Gigatronics 2550B signal generator. The power meter was calibrated at VTT MIKES within a few weeks prior to the measurements reported in this article.

REFERENCES

- R. F. Clark, *Proc. IEEE* **74**, 102 (1986).
- C. L. Holloway, M. T. Simons, M. D. Kautz, A. H. Haddab, D. Novotny, J. H. Lehman, P. A. Williams, and G. A. Shaw, *Appl. Phys. Lett.* **113**, 164102 (2018).
- C. L. Holloway, M. T. Simons, J. A. Gordon, P. F. Wilson, C. M. Cooke, D. A. Anderson, and G. Raithel, *IEEE Trans. Electromagn. Compat.* **59**, 717 (2017).
- A. Huber, K. McCormick, P. Andrew, P. Beaumont, S. Dalley, J. Fink, J. C. Fuchs, K. Fullard, W. Fundamenski, L. C. Ingesson, F. Mast, S. Jachmich, G. F. Matthews, P. Mertens, V. Philipps, R. A. Pitts, S. Sanders, and W. Zeidner, *Fusion Eng. Des.* **82**, 1327 (2007).
- C. Pradere, J.-P. Caumes, J. Toutain, E. Abraham, B. Chassagne, and J.-C. Batsale, *Appl. Opt.* **52**, 2320 (2013).
- N. Ahr and E. Tegeler, *Nucl. Instrum. Methods Phys. Res., Sect. A* **319**, 387 (1992).
- G. S. Tucker, J. B. Peterson, C. B. Netterfield, E. L. Griffith, and G. S. Griffin, *Rev. Sci. Instrum.* **65**, 301 (1994).
- J. T. Dempsey, P. Friberg, T. Jenness, R. P. J. Tilanus, H. S. Thomas, W. S. Holland, D. Bintley, D. S. Berry, E. L. Chapin, A. Chrysostomou, G. R. Davis, A. G. Gibb, H. Parsons, and E. I. Robson, *Mon. Not. R. Astron. Soc.* **430**, 2534 (2013).
- D. Schwan, P. A. R. Ade, K. Basu, A. N. Bender, F. Bertoldi, H.-M. Cho, G. Chon, J. Clarke, M. Dobbs, D. Ferrusca, R. Güsten, N. W. Halverson, W. L. Holzapfel, C. Horellou, D. Johansson, B. R. Johnson, J. Kennedy, Z. Kermish, R. Kneissl, T. Lanting, A. T. Lee, M. Lueker, J. Mehl, K. M. Menten, D. Muders, F. Pacaud, T. Plagge, C. L. Reichardt, P. L. Richards, R. Schaaf, P. Schilke, M. W. Sommer, H. Spieler, C. Tucker, A. Weiss, B. Westbrook, and O. Zahn, *Rev. Sci. Instrum.* **82**, 091301 (2011).
- A. Avella, G. Brida, I. P. Degiovanni, M. Genovese, M. Gramegna, L. Lolli, E. Monticone, C. Portesi, M. Rajteri, M. L. Rastello *et al.*, *Opt. Express* **19**, 23249 (2011).
- C. Arnaboldi, S. Capelli, O. Cremonesi, L. Gironi, M. Pavan, G. Pessina, and S. Pirro, *Astropart. Phys.* **34**, 344 (2011).
- J. S. Cushman, A. Dally, C. J. Davis, L. Ejzak, D. Lenz, K. E. Lim, K. M. Heeger, R. H. Maruyama, A. Nucciotti, S. Sangiorgio, and T. Wise, *Nucl. Instrum. Methods Phys. Res., Sect. A* **844**, 32 (2017).
- A. H. Abdelhameed, S. V. Bakhlanov, P. Bauer, A. Bento, E. Bertoldo, L. Canonica, A. V. Derbin, I. S. Drachnev, N. F. Iachellini, D. Fuchs, D. Hauff, M. Laubenstein, D. A. Lis, I. S. Lomskeya, M. Mancuso, V. N. Muratova, S. Nagorny, S. Nisi, F. Petricca, F. Proebst, J. Rothe, V. V. Ryabchenkov, S. E. Sarkisov, D. A. Semenov, K. A. Subbotin, M. V. Trushin, E. V. Unzhakov, and E. V. Zharikov, *Eur. Phys. J. C* **80**, 376 (2020).
- D. D. Dinh, “Millimetre-wave power sensor design,” Ph.D. thesis, University of Birmingham, 2017.
- J. C. Bardin, D. H. Slichter, and D. J. Reilly, *IEEE J. Microwaves* **1**, 403 (2021).
- F. Yan, D. Campbell, P. Krantz, M. Kjaergaard, D. Kim, J. L. Yoder, D. Hover, A. Sears, A. J. Kerman, T. P. Orlando, S. Gustavsson, and W. D. Oliver, *Phys. Rev. Lett.* **120**, 260504 (2018).
- S. Krinner, S. Storz, P. Kurpiers, P. Magnard, J. Heinsoo, R. Keller, J. Lütolf, C. Eichler, and A. Wallraff, *EPJ Quantum Technol.* **6**, 2 (2019).
- A. Vaaranta, M. Cattaneo, and R. E. Lake, *Phys. Rev. A* **106**, 042605 (2022).
- L. Ranzani, L. Spietz, Z. Popovic, and J. Aumentado, *Rev. Sci. Instrum.* **84**, 034704 (2013).
- S. Simbierowicz, V. Y. Monarkha, S. Singh, N. Messaoudi, P. Krantz, and R. E. Lake, *Appl. Phys. Lett.* **120**, 054004 (2022).
- E. Hyyppä, M. Jenei, S. Masuda, V. Sevriuk, K. Y. Tan, M. Silveri, J. Goetz, M. Partanen, R. E. Lake, L. Grönberg, and M. Möttönen, *Appl. Phys. Lett.* **114**, 192603 (2019).
- A. Blais, S. M. Girvin, and W. D. Oliver, *Nat. Phys.* **16**, 247 (2020).
- G. Wendin, *Rep. Prog. Phys.* **80**, 106001 (2017).
- M. H. Devoret, A. Wallraff, and J. M. Martinis, *arXiv:cond-mat/0411174* (2004).
- P. Krantz, M. Kjaergaard, F. Yan, T. P. Orlando, S. Gustavsson, and W. D. Oliver, *Appl. Phys. Rev.* **6**, 021318 (2019).
- S. Kwon, A. Tomonaga, G. Lakshmi Bhai, S. J. Devitt, and J.-S. Tsai, *J. Appl. Phys.* **129**, 041102 (2021).
- A. Blais, A. L. Grimsmo, S. M. Girvin, and A. Wallraff, *Rev. Mod. Phys.* **93**, 025005 (2021).
- J. Tuorila, M. Silveri, M. Sillanpää, E. Thuneberg, Y. Makhlin, and P. Hakonen, *Phys. Rev. Lett.* **105**, 257003 (2010).
- J. Gambetta, A. Blais, D. I. Schuster, A. Wallraff, L. Frunzio, J. Majer, M. H. Devoret, S. M. Girvin, and R. J. Schoelkopf, *Phys. Rev. A* **74**, 042318 (2006).
- R. Dassonneville, R. Assouly, T. Peronnin, P. Rouchon, and B. Huard, *Phys. Rev. Appl.* **14**, 044022 (2020).
- S. Kono, K. Koshino, Y. Tabuchi, A. Noguchi, and Y. Nakamura, *Nat. Phys.* **14**, 546 (2018).
- J.-C. Besse, S. Gasparinetti, M. C. Collodo, T. Walter, P. Kurpiers, M. Pechal, C. Eichler, and A. Wallraff, *Phys. Rev. X* **8**, 021003 (2018).
- E. Albertinale, L. Balembois, E. Billaud, V. Ranjan, D. Flanigan, T. Schenkel, D. Estève, D. Vion, P. Bertet, and E. Flurin, *Nature* **600**, 434 (2021).
- E. Flurin, N. Roch, J. D. Pillet, F. Mallet, and B. Huard, *Phys. Rev. Lett.* **114**, 090503 (2015).

- ³⁵J. Wenner, Y. Yin, Y. Chen, R. Barends, B. Chiaro, E. Jeffrey, J. Kelly, A. Megrant, J. Y. Mutus, C. Neill, P. J. J. O'Malley, P. Roushan, D. Sank, A. Vainsencher, T. C. White, A. N. Korotkov, A. N. Cleland, and J. M. Martinis, *Phys. Rev. Lett.* **112**, 210501 (2014).
- ³⁶P. Schmidt, D. Schwienbacher, M. Pernpointner, F. Wulschner, F. Deppe, A. Marx, R. Gross, and H. Huebl, *Appl. Phys. Lett.* **113**, 152601 (2018).
- ³⁷A. Schneider, J. Braumüller, L. Guo, P. Stehle, H. Rotzinger, M. Marthaler, A. V. Ustinov, and M. Weides, *Phys. Rev. A* **97**, 062334 (2018).
- ³⁸M. Kristen, A. Schneider, A. Stehli, T. Wolz, S. Danilin, H. S. Ku, J. Long, X. Wu, R. Lake, D. P. Pappas, A. V. Ustinov, and M. Weides, *npj Quantum Inf.* **6**, 57 (2020).
- ³⁹T. Hönigl-Decrinis, R. Shaikhaidarov, S. E. de Graaf, V. N. Antonov, and O. V. Astafiev, *Phys. Rev. Appl.* **13**, 024066 (2020).
- ⁴⁰M. Jerger, A. Kulikov, Z. Vasselin, and A. Fedorov, *Phys. Rev. Lett.* **123**, 150501 (2019).
- ⁴¹M. Scigliuzzo, A. Bengtsson, J.-C. Besse, A. Wallraff, P. Delsing, and S. Gasparinetti, *Phys. Rev. X* **10**, 041054 (2020).
- ⁴²R. Kokkonen, J.-P. Girard, D. Hazra, A. Laitinen, J. Govenius, R. E. Lake, I. Sallinen, V. Vesterinen, M. Partanen, J. Y. Tan, K. W. Chan, K. Y. Tan, P. Hakonen, and M. Möttönen, *Nature* **586**, 47 (2020).
- ⁴³G.-H. Lee, D. K. Efetov, W. Jung, L. Ranzani, E. D. Walsh, T. A. Ohki, T. Taniguchi, K. Watanabe, P. Kim, D. Englund, and K. C. Fong, *Nature* **586**, 42 (2020).
- ⁴⁴S. Pirro and P. Mauskopf, *Ann. Rev. Nucl. Part. Sci.* **67**, 161–181 (2017).
- ⁴⁵V. Lubсанov, V. Gurtovoi, A. Semenov, E. Glushkov, V. Antonov, and O. Astafiev, *Supercond. Sci. Technol.* **35**, 105013 (2022).
- ⁴⁶F. Paolucci, N. Ligato, G. Germanese, V. Buccheri, and F. Giazotto, *Appl. Sci.* **11**, 746 (2021).
- ⁴⁷F. Giazotto, T. T. Heikkilä, A. Luukanen, A. M. Savin, and J. P. Pekola, *Rev. Mod. Phys.* **78**, 217 (2006).
- ⁴⁸D. R. Schmidt, C. S. Yung, and A. N. Cleland, *Appl. Phys. Lett.* **83**, 1002 (2003).
- ⁴⁹J. Govenius, R. E. Lake, K. Y. Tan, and M. Möttönen, *Phys. Rev. Lett.* **117**, 030802 (2016).
- ⁵⁰J. Govenius, R. E. Lake, K. Y. Tan, V. Pietilä, J. K. Julin, I. J. Maasilta, P. Virtanen, and M. Möttönen, *Phys. Rev. B* **90**, 064505 (2014).
- ⁵¹R. Kokkonen, J. Govenius, V. Vesterinen, R. Lake, A. Gunyhó, K. Tan, S. Simbierowicz, L. Grönberg, J. Lehtinen, M. Prunnila *et al.*, *Commun. Phys.* **2**, 124 (2019).
- ⁵²P. Dubos, H. Courtois, B. Pannetier, F. K. Wilhelm, A. D. Zaikin, and G. Schön, *Phys. Rev. B* **63**, 064502 (2001).
- ⁵³R. E. Lake, J. Govenius, R. Kokkonen, K. Y. Tan, M. Partanen, P. Virtanen, and M. Möttönen, *Adv. Electron. Mater.* **3**, 1600227 (2017).
- ⁵⁴C. T. Ke, I. V. Borzenets, A. W. Draelos, F. Amet, Y. Bomze, G. Jones, M. Craciun, S. Russo, M. Yamamoto, S. Tarucha, and G. Finkelstein, *Nano Lett.* **16**, 4788 (2016).
- ⁵⁵S. Guéron, H. Pothier, N. O. Birge, D. Esteve, and M. H. Devoret, *Phys. Rev. Lett.* **77**, 3025 (1996).
- ⁵⁶J. C. Hammer, J. C. Cuevas, F. S. Bergeret, and W. Belzig, *Phys. Rev. B* **76**, 064514 (2007).
- ⁵⁷M. Tinkham, *Introduction to Superconductivity*, 2nd ed. (Dover Publications, 2004).
- ⁵⁸P. Virtanen, F. S. Bergeret, J. C. Cuevas, and T. T. Heikkilä, *Phys. Rev. B* **83**, 144514 (2011).
- ⁵⁹C. Song, T. W. Heitmann, M. P. DeFeo, K. Yu, R. McDermott, M. Neeley, J. M. Martinis, and B. L. T. Plourde, *Phys. Rev. B* **79**, 174512 (2009).
- ⁶⁰H. Pothier, S. Guéron, N. O. Birge, D. Esteve, and M. H. Devoret, *Phys. Rev. Lett.* **79**, 3490 (1997).
- ⁶¹J.-P. Girard, R. E. Lake, W. Liu, R. Kokkonen, E. Visakorpi, J. Govenius, and M. Möttönen (2023), "Datasets for Cryogenic sensor enabling broad-band and traceable power measurements," Zenodo. <https://doi.org/10.5281/zenodo.7804794>
- ⁶²A. B. Zorin, *Rev. Sci. Instrum.* **66**, 4296 (1995).
- ⁶³"Keysight 2-port and 4-port pna-x network analyzer - technical specifications," <https://www.keysight.com/fit/en/assets/9018-04526/technical-specifications/9018-04526.pdf>, 2023.
- ⁶⁴J. A. Brevik, A. S. Boaventura, A. A. Babenko, M. A. Castellanos-Beltran, N. E. Flowers-Jacobs, A. E. Fox, P. F. Hopkins, P. D. Dresselhaus, D. F. Williams, and S. P. Benz, in *2020 Conference on Precision Electromagnetic Measurements (CPEM, 2020)*, pp. 1–2.
- ⁶⁵J. Burnett, A. Bengtsson, D. Niepce, and J. Bylander, *J. Phys.: Conf. Ser.* **969**, 012131 (2018).
- ⁶⁶A. M. Gunyhó, S. Kundu, J. Ma, W. Liu, S. Niemelä, G. Catto, V. Vadimov, V. Vesterinen, P. Singh, Q. Chen, and M. Möttönen, [arXiv:2303.03668](https://arxiv.org/abs/2303.03668) (2023).
- ⁶⁷J. T. Peltonen, P. Virtanen, M. Meschke, J. V. Koski, T. T. Heikkilä, and J. P. Pekola, *Phys. Rev. Lett.* **105**, 097004 (2010).
- ⁶⁸E. Strambini, F. S. Bergeret, and F. Giazotto, *Appl. Phys. Lett.* **105**, 082601 (2014).